UNIVERSITY OF TRIESTE

DEPARTMENT OF PHYSICS

Bachelor's degree in Physics

Bachelor's Thesis

# Commissioning of an infrared spectrometer for applications in optical pump and probe experiments

**Supervisor**
prof. Daniele Fausti

**Cosupervisors:**
Francesca Giusti, PhD
Angela Montanaro

**Candidate**
Jacopo De Santis

Academic year 2019-2020

UNIVERSITÀ DEGLI STUDI DI TRIESTE

DIPARTIMENTO DI FISICA

Corso di Laurea Triennale in Fisica

Tesi di Laurea Triennale

# Implementazione di uno spettrometro infrarosso per applicazioni in esperimenti di pump & probe ottico

**Supervisor**
prof. Daniele Fausti

**Cosupervisors:**
dott.ssa Francesca Giusti
dott.ssa Angela Montanaro

**Candidate**
Jacopo De Santis

Anno accademico 2019-2020

## Abstract

La superconduttività a temperature critiche prossime a quella ambiente può essere considerata il sacro Graal della fisica della materia condensata. Ad oggi, trascurando il caso dell' idruro di zolfo carbonioso ad elevatissime pressioni [1], i materiali che hanno mostrato comportamento superconduttivo alle temperature più elevate (fino ad un massimo di −135 °C) appartengono alla famiglia dei cuprati (ossidi di rame). Sfortunatamente, il meccanismo che porta alla superconduttività a tali temperature non è ancora compreso, di qui il bisogno di indagarlo più a fondo.

Uno dei principali strumenti per lo studio della superconduttività nei cuprati sono gli esperimenti di *Pump & probe*, tecniche di spettroscopia ottica ultraveloce risolte in tempo che permettono, attraverso lo studio delle dinamiche ottiche del campione nelle regioni del visibile e del vicino infrarosso, di andare ad individuare le transizioni alla fase superconduttiva permettendo di separare i diversi contributi provenienti dai vari gradi di libertà [2]. In particolare, nei precedenti lavori del gruppo presso il quale è stata svolta questa tesi sono stati condotti svariati esperimenti utilizzando un probe a banda larga nel visibile (che permette quindi di monitorare la dipendenza temporale della risposta spettrale delle transizioni ottiche a più alta energia e vicine al charge transfer nei cuprati) [3, 4]. Tuttavia, lo studio della risposta ottica a più basse energie (nel vicino infrarosso), che è meno comune perché richiede una tecnologia di acquisizione non basata sul silicio e che abbia un'elettronica di acquisizione sufficientemente veloce, permette invece di monitorare come l'accoppiamento tra i gradi di libertà elettronici e gli altri bosonici caratteristici del materiale (magnetici, vibrazionali...) vengono modificati a seguito della fotoeccitazione.

Per fare questo secondo tipo di misure è necessario innanzitutto avere un detector adatto: in questo lavoro di tesi verrà quindi presentata l' implementazione di uno spettrometro infrarosso per applicazioni in esperimenti di *Pump & probe* ottico. Dopo la descrizione di tali esperimenti e dei fenomeni di ottica non lineare sfruttati per la realizzazione del setup in uso (capitolo 2), mi concentrerò sul commissioning dello spettrometro, fornendo un'analisi approfondita della sua struttura e delle sue componenti e spiegando in che modo abbiamo integrato il suo processo di acquisizione all'interno della scansione temporale di un esperimento di *Pump & probe* (capitolo 3). Successivamente, riporterò un set di misure effettuate per caratterizzare la risposta dello spettrometro (capitolo 4) ed infine presenterò i risultati di un esperimento di *Pump & probe* a temperatura ambiente condotto su un campione di BSCCO in condizioni di doping ottimale (capitolo 5).

# Contents

# Chapter 1

# Introduction: Why study cuprates with an IR probe

Room-temperature superconductivity can be considered the holy grail of condensed matter physics. Indeed, if it was achieved, its technological application would bring humanity to a next development stage with efficient quantum computers, cost effective mag-lev bullet trains, dissipationless transmission lines, feasible magnetic plasma confinement in fusion reactors and more. As of today, neglecting the extremely pressurized carbonaceous sulfur hydride [1], the materials that show superconducting behaviour at the highest temperature (as high as $-135\,^{\circ}\mathrm{C}$) are cuprates. Unfortunately, their working mechanism is still not understood, hence the need of further studies.

## Superconductivity

Superconductivity was first discovered by Kamerlingh-Onnes in 1911 [5], when he observed that at very low temperatures (below $4.2\,\mathrm{K}$) the resistivity of mercury fell to unmeasurable values. In the following years, it was found that this property was not unique to mercury, indeed a quite wide class of elements showed the same behaviour when cooled at the temperature of liquid helium. Hence, this class of materials was named "superconductors".

The superconducting phenomenon was explained only 46 years later, by Bardeen Cooper and Schrieffer. In their model (named BCS model after their initials) the key phenomenon that brings to superconductivity is the pairing of electrons. This pairing consists in the establishment of an attractive potential between two electrons with opposite spin. This brings to the transformation of two fermions with opposite spins (the electrons) into a single bosonic particle (the bound pair) which is called Cooper pair. Being bosons of spin zero, Cooper pairs obey the Bose-Einstein statistics, hence one state can be occupied by an infinite number of pairs. In BCS theory, the electron-electron attraction which brings to the pairing is mediated by a phonon, in other words it is due to electron-lattice interaction in the solid.

## High temperature superconductors: cuprates

In 1986 Bednorz and Müller observed that the $La_{1.85}Ba_{0.15}CuO_4$ showed superconductive behaviour at a temperature of 30 K, noticeably higher than the critical temperature of the known superconductors [6]. This discovery opened up to the definition of a new class of materials: "high temperature superconductors". Indeed, the electron pairing mediated by phonon of BCS theory is too weak to explain superconductivity at such high temperatures, hence the formation of the superconducting state has to be determined by a different mechanism. To date, there is still no organic quantum description of the electronic dynamics that leads to the formation of Cooper pairs in high temperature superconductors.
Many of the most studied high temperature superconductors (like $La_2CuO_4$ itself) belong to the class of copper oxides, or cuprates. They all have a layered structure whose main structural unit, which is typical of the whole family, are the Cu-O planes, which act as conducting planes, separated by insulating planes, which act as charge reservoirs (see figure 1.1).

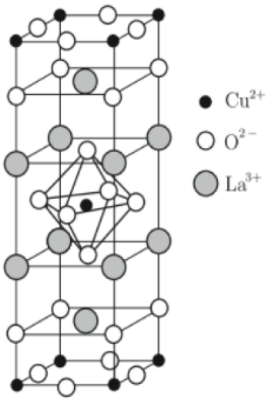

Figure 1.1: $La_2CuO_4$ crystalline structure, which is representative of the whole class of cuprates.

Without any doping, cuprates are Mott insulators and this does not allow the superconducting transition. But when opportunely doped (for example with the substitution of doping cations like Barium or Strontium), carriers appear in the conducting Cu-O planes, allowing conductivity and superconductivity. The superconductivity in cuprates is intrinsically related to the carriers concentration, hence to the percentage of doping cations. In particular, the critical temperature for superconductivity is maximized for a characteristic level of doping. Such compounds are called optimally doped.

## Pump & probe experiments on cuprates

Pump and probe experiments are a fundamental tool in the study of the mechanism that is responsible for electron pairing in unconventional superconductors like cuprates. In these experiments, an ultrashort intense pulse is used to excite the sample generating a non-equilibrium state whose relaxation process is studied by monitoring the time-evolution of the sample's optical properties (like reflectivity or transmissivity) by means of a second weaker pulse. This allows the observation of the sub-picosecond dynamics of impulsively excited states which can be both used to disentangle, due to their different dynamics, the different types of bosonic excitations that leads to the pairing of electrons, and to coherently manipulate the superconducting condensate through the photoinjection of short, intense laser pulses [2]. In particular, in a recent work from the hosting research group of this thesis, signatures of an enhancement of critical superconductivity temperature driven by mid infrared pulse excitations have been found [7].
A debated peculiarity of cuprates is that the transition to the superconducting phase seems to correspond to a change of spectral weight at energies of the order of eV (hundreds of times bigger than the superconducting gap, which is of the order of tens of meV) [4, 8]. This behaviour is visible in *Pump & probe* experiments with probes in the near infrared region. Indeed, the study of the optical response at such energies allows to monitor how the couplings between electronic and bosonic degrees of freedom in the material are modified by photoexcitation.
To do so, it is necessary to have a suitable near infrared detector. Hence, in this thesis work the commissioning of an infrared spectrometer for applications in optical *Pump & probe* experiments will be reported.

## Reading guide

After describing *Pump & probe* experiments and the non-linear phenomena that are exploited for the realization the setup used (chapter 2), I will focus on the commissioning of the spectrometer, giving a deep analysis of its structure and its components and explaining how we integrated its acquisition in the timing of a *Pump & probe* experiment (chapter 3). Then I will present a set of measurements performed to characterize the spectrometer's response (chapter 4) and lastly I will show and comment the results obtained from a *Pump & probe* measuring session with the spectrometer on an optimally doped BSCCO sample at room temperature (chapter 5).

# Chapter 2

# Experimental techniques

In this chapter I will introduce non equilibrium optical experiments. To study a material out of equilibrium, it is essential to apply external stimulations faster than the relaxation time of the sample. In condensed matter physics, these times are mainly at sub-nanosecond timescales [2]. Hence, their study is feasible only thanks to the use of ultrafast laser sources, which deliver ultrashort, coherent light pulses with duration of the order of $(1-100)\,\mathrm{fs}$.

In particular, I will focus my attention on *Pump & probe* experiments. After describing the main ideas on which they are based (section 2.1), I will show how they are realized, focusing on the optical effects exploited for their realization (section 2.2) and describing the experimental set up we used (section 2.3).

## 2.1 Pump & probe spectroscopy

*Pump & probe* is a time-resolved spectroscopic technique which is used to study non-equilibrium dynamics in materials. The main idea is quite simple: the sample is perturbed by an intense ultrashort light pulse called *pump*, then a weaker pulse (the *probe*) is used to monitor the time-evolution of the optical properties of the sample. Usually, the optical property monitored is the reflectivity (or the transmissivity) of the sample (see figure 2.1).

In particular, the percentage difference between the reflectivity in the presence of the pump ($R_{ex}$) and in the absence of it ($R_{eq}$) is measured as a function of the time delay between the pump and the probe. This quantity is called transient reflectivity.

$$\frac{\delta R}{R}(t) = \frac{R_{ex}(t) - R_{eq}}{R_{eq}} \tag{2.1}$$

The delay $t$ is typically tuned by varying the length of the optical path of one of the two pulses by means of a micrometer translation stage. Indeed, with a path difference sensitivity $\Delta l = 1\,\mu\mathrm{m}$ it is possible to tune the delay between the two

pulses with a temporal sensitivity of $\Delta t = \frac{\Delta l}{c} \simeq 3.3\,\mathrm{fs}$, which is enough to study electronic relaxation processes.
Of course, there are many factors that influence the response of the sample, both on the *pump* characteristics (intensity, spectral content, polarization, temporal length) and on the sample conditions (temperature, pressure). This versatility is particularly useful for the study of complex materials (materials with several interplaying degrees of freedom),in order to be able to excite and then disentangle due to the different relaxation times, their different degrees of freedom.
Being more specific, in our experimental setup (which will be analyzed in detail in section 2.3), we used a tunable wavelength quasi-monochromatic pump in order to be able to address different excitations by being in resonance with specific transitions and a broadband white light probe, which allows us to measure the transient reflectivity on a spectral region which covers different optical transition giving us the ability to reconstruct the temporal dynamics of the dielectric function of the sample.
These two different pulses are obtained from the same laser beam exploiting nonlinear optical effects, which will be described in the next section.

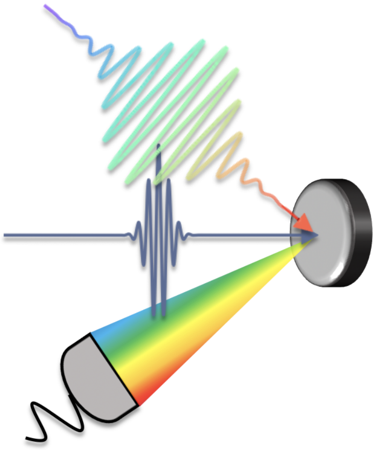

Figure 2.1: Sketch of a broadband optical *Pump & probe* experiment. The pump pulse excites the sample and then, after a time delay t, the white light probe pulse is reflected by the sample. Finally the reflected broadband probe's spectral content is analyzed by a spectrometer.

## 2.2 Non-linear optical effects for ultrafast spectroscopy

As we will see in detail in the description of the experimental setup (section 2.3), a consistent part of the instrumentation used takes advantage of nonlinear optical effects. In this section I will then provide an overview of the main phenomena exploited.

**Nonlinear polarization**

In low-field approximation a good description of light-matter interaction is given by a linear dependence of the medium's polarization from the external field

$$\mathbf{P} = \epsilon_0 \chi \mathbf{E} \tag{2.2}$$

But when using laser pulses, due to the high intensity of the fields involved, this description is no longer valid. The electric susceptibility can no longer be considered a constant: in this regime it is a function of the electric field $\chi = \chi(\mathbf{E})$. Expanding the susceptibility tensor to the second order about $E = 0$ we obtain

$$\chi_{ij}(\mathbf{E}) \simeq \chi_{ij}(0) + \frac{\partial \chi_{ij}}{\partial E_k}(0) E_k + \frac{1}{2} \frac{\partial^2 \chi_{ij}}{\partial E_k \partial E_l}(0) E_k E_l \tag{2.3}$$

which substituted in (1.2) gives

$$P_i \simeq \epsilon_0 \chi_{ij}^{(1)} E_j + \epsilon_0 \chi_{ijk}^{(2)} E_j E_k + \epsilon_0 \chi_{ijkl}^{(3)} E_j E_k E_l \tag{2.4}$$

We can then identify the nonlinear polarization components[1]

$$P \simeq P^{(1)} + P^{(2)} + P^{(3)} \tag{2.5}$$

A detailed description of nonlinear effects is not the aim of this work, hence in the following subsections I will provide a simplified description of these effects, focusing the attention on the ones which find useful and broad application in *Pump & probe* experimental setups.

### 2.2.1 Second order effects

Approaching the argument in an intuitive way [9], we can consider an external electric field given by two incident plain waves

$$E = \varepsilon_1 \cos(\omega_1 t) + \varepsilon_2 \cos(\omega_2 t) \tag{2.6}$$

---

[1] Written for scalar quantities, for the sake of simplicity.

Substituting in the expression for $P^{(2)}$ in eq 2.4, we obtain

$$P^{(2)} = \frac{\epsilon_0}{2}\chi^{(2)}\varepsilon_1\varepsilon_2[\cos(\omega_1+\omega_2)t + \cos(\omega_1-\omega_2)t] \tag{2.7}$$

Hence, second order nonlinear response generates polarization terms which oscillate at the frequencies of

$$\begin{aligned} \omega_{sum} &= \omega_1 + \omega_2 \\ \omega_{diff} &= |\omega_1 - \omega_2| \end{aligned} \tag{2.8}$$

So, in the response field of a medium stimulated by two waves of frequency $\omega_1$ and $\omega 2$ there are also components which oscillates at $\omega_{sum}$ (sum frequency mixing) and at $\omega_{diff}$ (difference frequency mixing).
Due to symmetry arguments, $\chi^{(2)}$ is zero for all centrosymmetric crystals, hence the typical nonlinear crystal used to exploit second order phenomena are birifrangent non-linear crystals, like the $\beta$-barium-borate (BBO).
In the following paragraphs, I will describe the two important effects of second order nonlinear response that are used in our setup.

### Second harmonic generation

If we consider a self-interacting field (*i.e.* $\omega_1 = \omega_2 = \omega$), from sum frequency mixing we obtain a response field oscillating at $2\omega$. We have then generated the second harmonic of the stimulating field.

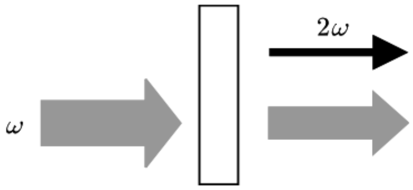

Figure 2.2: Second harmonics generation scheme (image from [9]).

### Optical parametric amplification

Optical parametric application consists in the amplification of a weak signal beam by nonlinear mixing with a strong pump beam. It can be described as a two stage difference wave mixing, mediated by idler photons at a third frequency such that

$$\omega_p = \omega_i + \omega_s \tag{2.9}$$

Firstly, the idler photons ($\omega_i = |\omega_p - \omega_s|$) are generated by difference wave mixing between pump and signal; then, by further mixing with the pump field, idler photons generate photons at frequency $\omega_s = |\omega_p - \omega_i|$.

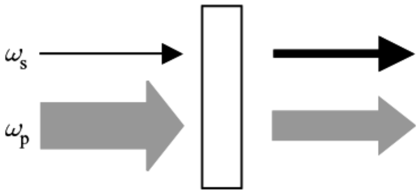

Figure 2.3: Optical parametric amplification scheme (image from [9]).

It is possible to transfer power from the pump to the signal beam with this phenomenon only if particular conditions on the relations within the orientations of the nonlinear crystal and the direction of the incident light beams are satisfied, hence the term parametric in the name. Indeed, usually, nonlinear effects are small, so that relatively long nonlinear media (with a length of the order of mm) are needed to obtain relevant conversion efficiencies. But this is possible only if the newly generated waves interfere constructively through the crystal, which happens if the waves have specific constant phase relations between them (phase matching conditions). [10]

### 2.2.2 Third order effects

The linear dielectric function is defined as

$$\epsilon_1 = \epsilon_0(1 + \chi^{(1)}) \tag{2.10}$$

Typically, the crystals used to exploit third order nonlinear effects are centrosymmetric (with $\chi^{(2)} = 0$).[2] Hence, introducing the first non-zero correction ($\chi^{(3)}$), we obtain the corrected dielectric function

$$\epsilon = \epsilon_1 + \epsilon_2 E^2 \tag{2.11}$$

Consequently, the refractive index contains a quadratic term in the electric field

$$n = n_0 + n_2 E^2 \tag{2.12}$$

This implies a dependence of the mean refractive index from the intensity of the incident radiation

$$n = n_0 + n_2 \langle E^2 \rangle = n_0 + \bar{n}_2 I \tag{2.13}$$

This phenomenon is called optical Kerr effect and it is the basis of the two most important processes that concur to the generation of white light pulses through the interaction between ultra-intense and ultra-short laser pulses and non-linear crystals.

---

[2] The most common ones are Yttrium Aluminium Garnet (YAG) and Aluminum Oxide (sapphire) crystals.

### Self focusing

Typically, a laser pulse has a gaussian transverse spatial profile

$$I(r) = I_0 e^{-\frac{r^2}{2\alpha^2}} \tag{2.14}$$

Due to the optical Kerr effect, the refraction index of the kerr-active medium is greater at the center of the section (if $\bar{n}_2 > 0$, as is in the most of kerr media). This fact makes the medium act as a converging lens and causes the pulse to collapse on itself (hence the term self focusing), as sketched in figure 2.3.

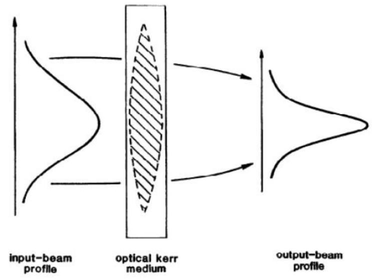

Figure 2.4: Self focusing of a beam due to its interaction with a Kerr medium (image from [11]).

### Self phase modulation

Self Phase Modulation is the temporal equivalent of the self focusing effect. Typically, a laser pulse has a gaussian temporal profile

$$I(t) = I_0 e^{-\frac{t^2}{\tau^2}} \tag{2.15}$$

Hence, the refractive index is time dependent

$$n(t) = n_0 + \bar{n}_2 I(t) \tag{2.16}$$

This implies a variation in the optical path L=nd, where $d$ is the thickness of the medium,

$$\Delta L = \bar{n}_2 d \cdot I(t) = \bar{n}_2 d \cdot I_0 e^{-\frac{t^2}{\tau^2}} \tag{2.17}$$

Consequently, we have a phase shift (considering a pulse of wavelength $\lambda_0$)

$$\Delta\phi = -\frac{2\pi\delta L}{\lambda_0} = \frac{2\pi\bar{n}_2 d}{\lambda_0} I_0 e^{-\frac{t^2}{\tau^2}} \tag{2.18}$$

But since we have $\omega := \frac{d\phi}{dt}$, this implies a dispersion in the instantaneous angular frequency

$$\Delta\omega(t) = \frac{4\pi\bar{n}_2 d}{\lambda_0}\frac{t}{\tau^2}I_0 e^{-\frac{t^2}{\tau^2}} \tag{2.19}$$

Hence, the front of the pulse is driven to higher frequencies, while the tail is driven to lower ones: this implies a temporal dispersion of the spectral content of the white pulse produced (called *chirp*) which is typically corrected with physical compensation or data post-processing.
Self phase modulation, which is enhanced by the self focusing of the beam, is the main responsible of the supercontinuum white light generation.

## 2.3 The experimental setup

The experimental setup used for the *Pump & probe* experiments is sketched in figure 2.4

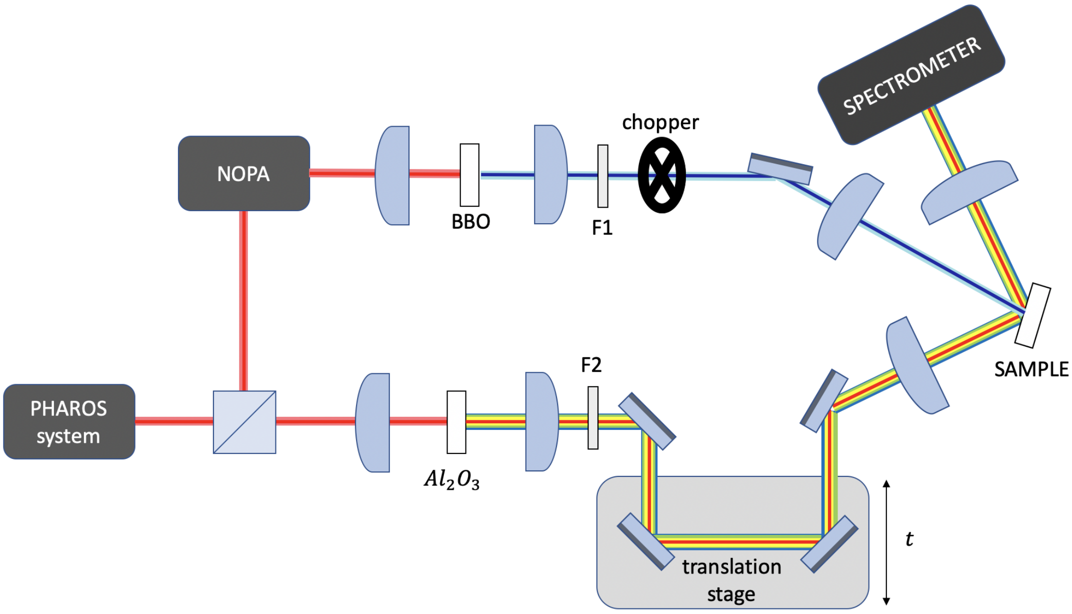

Figure 2.5: Schematic representation of the experimental setup. A detailed description of the optical arrangement is in the text.

The 1030 nm laser pulses generated by the pharos system are split in two beams by a beam splitter. The first one is modified by the NOPA and a second harmonic generation process to generate the visible pump beam (in blue). The second one is used to generate a supercontinuum probe beam on a sapphire crystal. A chopping

system is used to obtain both pumped and unpumped measurements, and a mechanical translation stage is used to modify the optical path of the probe to control the temporal delay between pumping and probing pulses.
I will now give a deeper insight of the different steps involved.

### 2.3.1 Laser source

The principal light source from which the pump and the probe beam are obtained is the *Pharos* laser system by *Light Conversion*. It is made of two main components: an oscillator and an amplifier. The oscillator generates femtosecond pulses through the technique of passive mode-locking, which consists in the self-packing of the light in the cavity due to the self-focusing effect (exposed in section 2.2.2). Then, the amplifier uses this pulses as seed for a chirped pulse amplification system to generate pulses with the following properties:

- pulse temporal length of 200 fs
- wavelength of 1030 nm
- repetition rate of 50 kHz (tunable with a built-in pulse picker)
- energy per pulse of 400 µJ

This beam is then split by a beam splitter to generate the pumping and the probing pulses.

### 2.3.2 Pump pulses

To generate visible pump pulses, the infrared beam from the Pharos system is used to pump an *Orpheus-N* by *Light Conversion*, which is a non collinear parametric optical amplifier (NOPA). This system exploits optical parametric amplification (see section 2.2.1) in a BBO crystal to generate output pulses with a tunable wavelength of $(650 - 900)\,\mathrm{nm}$. This tunability is achieved thanks to the use of white light (obtained through non-linear effects in a sapphire crystal) as seed. By changing the phase matching conditions between the white light and the pump on the BBO crystal indeed it is possible to select which wavelength is efficiently amplified. The peculiarity of this system is that pumping and signal beam (see figure 2.2) are not parallel, hence idler and signal are geometrically separated; moreover, the non collinearity broadens the bandwidth of the quasi-monochromatic output, allowing to obtain shorter pulses (up to less than 30 fs of temporal length [12]). To obtain higher photon energies, the beam exiting from the NOPA is then focused on a BBO crystal where it undergoes a second harmonic generation process (see section 2.2.1). In order to measure the transient reflectivity of eq 2.1, it is necessary to detect the reflectivity of the sample both in the presence and in the absence of the pump pulses' excitation. To do so, an optical chopper is inserted in the pump beam path. This device, consists in a rotating pierced disk which interrupts the light beam at regular time intervals with programmable frequency. If the chopping frequency is half of the measurement rate, this allows to alternate pumped and unpumped measurements.

The pump beam is then finally focused on the sample.

### 2.3.3 Supercontinuum probe pulses

In our experiments, the probe is a broadband ultrashort pulse. This allows us to measure the wavelength dependent response of the sample on a large spectral range with only one measurement.

To obtain a white light probe, the beam from the Pharos system is focused on a sapphire crystal, where the concurring effects of self phase modulation and self focusing lead to a frequency broadening.

The probe beam then covers a mechanically variable optical path before being focused on the sample, as we already pointed out. In the end, after the reflection on the sample, the spectral content of the probe beam is measured with a spectrometer (which will be analyzed in detail in the next chapter).

# Chapter 3

# The infrared spectrometer

In this chapter I will focus on the device commissioned during this thesis work, an *Hamamatsu Mini-spectrometer TG series cooled*. It is an optical spectrometer, a device used to analyze the spectral composition of a light beam, able to resolve a spectrum ranging from 900 nm to 2500 nm. In the following sections, will describe its components, its working principles (section 3.1) and its integration in the experimental setup (section 3.2). In particular, i took care of the realization of a LabVIEW program which would allow the user both to use the device as an independent tool and to integrate it in more complex *Pump & probe* setups.

## 3.1 The device and its components

The *Hamamatsu Mini-spectrometer TG series cooled* is an optical spectrometer whose working principle is based on the spatial dispersion of the light pulse.

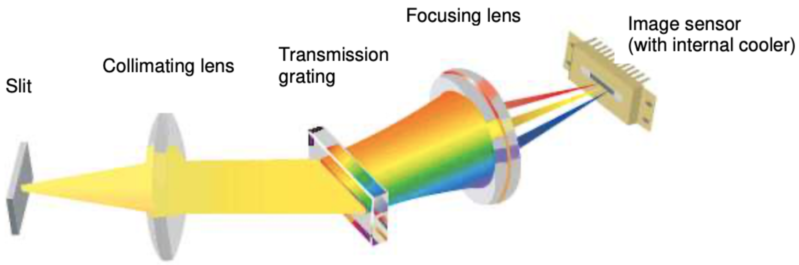

Figure 3.1: Optical spectrometer's working principle (image from [13]). The light beam entering the device through the slit is collimated by a lens in order to allow the spatial separation of its spectral content by means of a diffraction grating. The resolved spectrum is then focused by a lens on an array of 256 sensors to be detected.

The light beam is channelled into the spectrometer by an optical fiber. Upon entering the entrance slit, it is collimated by a lens and then its spectral content is spatially separated by the means of a dispersive element, consisting in a diffraction grating. The spatially resolved spectrum is then focused by a lens on an array of 256 sensors. Knowing the wavelength dependence of the response of the diodes, the spectral content of the light is resolved in intensity by the one to one correspondence between the position of the diode (pixel number) and the wavelength of the light incident on that sensor. From the theory of diffraction this relation is not linear [14], so the constructor provides the "calibration coefficients" by means of a polynomial up to the fifth order.

## The near infrared sensor

The technological heart of the spectrometer is its near infrared sensor. Indeed, infrared light is hard to detect due intrinsically low photon energy associated to this region of the light spectrum.
Based on the type of light-matter interaction they use, we can identify two main families of infrared detectors:

- Thermal type detectors
- Quantum type detectors

Thermal type detectors exploit thermal effects caused by the heating of the material due to the absorption of infrared incident light like the change of internal polarization (pyroelectric detectors) or the change of electric resistance (bolometers). These detectors have a wavelength independent response and work at room temperature, but they have a slow responsive time (of the order of ms) which makes them unsuitable for time resolved spectroscopy (sub-ps dynamics) [15].
Quantum type detectors exploit the photoexcitation of electrons to the conduction band in semiconductors. Unlike thermal effects, photoexcitation is based on single electron-photon interactions (it sees the radiation as quantized), hence it is wavelength dependent (see figure 3.2). In particular, there are two different effects that allow to convert photoexcited electrons into a sensible photocurrent: the photovoltaic effect, which consists in the generation of a photocurrent due to the space-charge field of a p-n junction, and the photoconductive effect, which consists in the reduction of the resistivity of the semiconductor due to excitation of more electrons in the conduction band [15]. The sensor we used is a photovoltaic one.
The amplitude of the energy gap between valence and conduction band determines the maximum detectable wavelength (cutoff) through the relation $\lambda_{co} \simeq \frac{hc}{E_{gap}}$.
The main advantage of these sensors is the high responsive speed [15], but due to the small band-gap needed to be able detect near infrared light, they are very noisy at room temperature. Typically, in order to reduce thermal fluctuations, they

are cooled to lower working temperatures by means of cooling systems like Peltier circuits (which will be described in the following paragraphs).

### InGaAs photodiode array on CMOS chip

The sensor we used is made of an array of extended InGaAs PIN photodiodes with a cutoff wavenlegth of 2.55 µm (0.45 eV). InGaAs is a semiconducting ternary alloy, whose typical cutoff wavelength is of 1.7 µm. However, by changing the composition ratio of this alloy, it is possible to further reduce the size of the energy gap, hence obtaining an extended version with a longer cutoff wavelength [16]. As we have already pointed out, the response of photodiodes is wavelength dependent. Figure 3.2 represents the spectral response of the sensor as declared from the constructor.

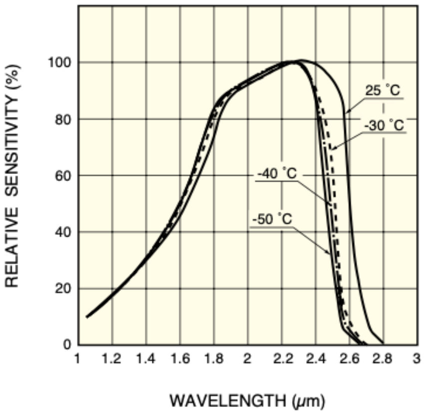

Figure 3.2: Spectral response of extended InGaAs PIN photodiodes at different operational temperatures as declared by the constructor (image from [16]). Between 1800 nm and 2400 nm the relative sensitivity is higher than 90% and then decreases rapidly to zero at the cutoff wavelength of 2500 nm. At lower wavelengths the sensitivity decrease is slower but still significant.

To complete the sensor, the InGaAs array is mounted on a complementary metal oxide semiconductor (CMOS) chip, which has for each pixel a transistor on which the electronics needed for the readout is formed (see figure 3.3). The diodes' response, after being amplified by a charge amplifier, is stored by the sample-and-hold circuit until a signal from the shift register orders to shift to the next acquisition. Then, the signal is passed through an address switch as an output. The timing of this processes is controlled by a timing generator, which interfaces with the clock (starting of the acquisition) and reset (ending of the acquisition) inputs from outside the sensor.

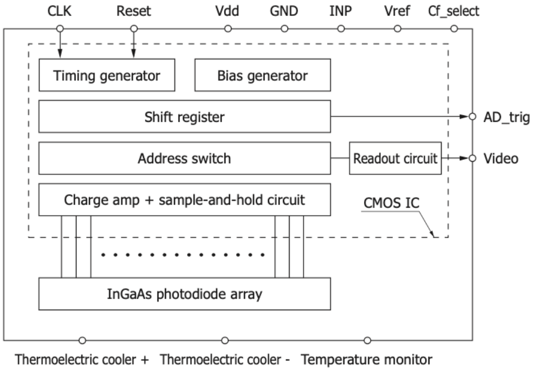

Figure 3.3: On-chip signal processing block diagram (image from [17]). The diodes' response is amplified by a charge amplifier and then stored by the sample-and-hold circuit until a signal from the shift register orders to shift to the next acquisition and pass the signal as an output through an address switch. The timing of this processes is controlled by a timing generator, which interfaces with the clock (starting of the acquisition) and reset (ending of the acquisition) external inputs.

### Peltier circuit

To reduce thermal noise and increase the signal-to-noise ratio, extended InGaAs photodiodes need to be cooled. To do so, the CMOS chip is connected to a thermoelectric cooler. Thermoelectric cooling is based on the Peltier effect, which is responsible for the absorption/emission (depending on the current direction) of heat at the junction of two conductors through which a DC electric current flows. This effect adds to the Joule effect and it is caused by the difference in the chemical potential in the two different metals forming the junction. [18]
Due to particular concurring phenomena, which is not the aim of this work to treat, p-n junctions are ideal to build thermoelectric refrigerators [18]. In particular, this spectrometer uses a two stage p-n thermoelectric cooler which is able to guarantee a constant working temperature of $-20\,^{\circ}\mathrm{C}$.

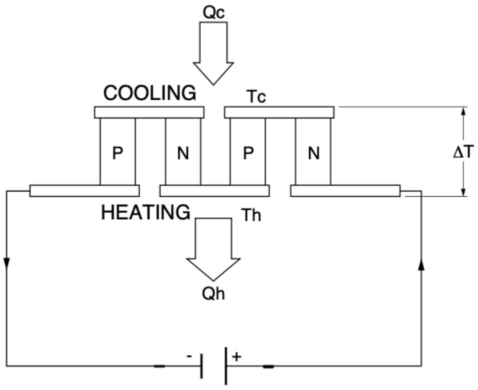

Figure 3.4: Sketch of the two stage Peltier circuit used to keep the sensor at −20 °C (image adapted from [16]). A DC current flows counterclockwise in the circuit, passing through the two p-n junctions in a direction such that the difference in chemicals potential between the two materials causes the absorption of heat from the end which is in thermal contact with the sensor.

## 3.2 Timing for the readout of the experiment

As we already discussed in section 2.3.2, to be able to measure both the pumped and the unpumped response of the sample in *Pump & probe* experiments, the optical chopper has to work at half of the acquisition frequency. But this is not enough. Indeed, in order to avoid "partially pumped" measurements, the chopper rotation and the acquisition of the spectrometer have to be synchronized. This is achievable thanks to the possibility of pairing both the chopper rotation and the clock and reset inputs of the time generators in the CMOS chip (figure 3.3) of the spectrometer to the same external signal (the trigger).

### 3.2.1 Operational modes of the spectrometer

The spectrometer has three main operational modes: continuous mode, specified mode and trigger mode (see figure 3.4). In continuous mode the beginning and the end of the measurement are controlled by computer commands; in specified mode, the beginning of the measurement is given by a coputer command, and then the process ends automatically after a predetermined number of acquisitions; in trigger mode the measurement process is controlled by an external electric signal called trigger. In order to be properly recognized, the trigger signal has to be a square wave with the following characteristics: a *low-level* of $(0-0.4)\,\mathrm{V}$; an *high-level* of $(4.75-5.25)\,\mathrm{V}$ and a *minimum width* of 200 ns [13].

Specified and continuous modes can be used to measure the spectral content of a light beam without needing precise time synchronization (for example to resolve the spectral content of the light beams of the set up like we will show in chapter

4); while trigger mode allows to synchronize the capture with other components of the experimental setup (exactly what is needed for *Pump & probe* experiments).

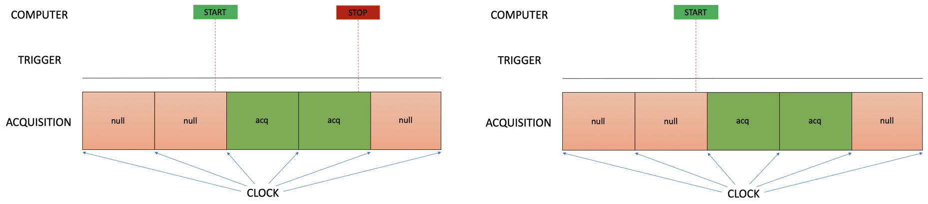

(a) *Continuous mode* (b) *Specified mode*

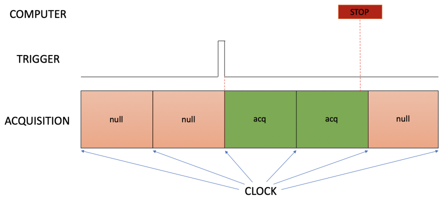

(c) *Trigger mode*

Figure 3.5: The three main operational modes. They differ for the type of control on measurement's beginning and end: computer controlled start and stop for continuous mode, computer controlled start and automatic stop for specified mode and external trigger start and computer controlled stop for trigger mode.

Trigger modes are further specified, so that the acquisition can be as flexible as possible.

### Software Trigger Vs External Trigger

In software trigger mode, the device uses a computer generated trigger. Since in *Pump & probe* experiments, we need to synchronize the acquisition with the pulses generation of the lasing system, this operational mode has not be used. In the external trigger mode, on the other hand, the device receives the trigger from external input (e.g. the trigger generated by the laser's electronics).

### Asynchronous Trigger Vs Synchronous Trigger

In asynchronous trigger mode the trigger signal is responsible only for the beginning of the acquisition. In this case the clock to the sensor is internally generated and is independent from the triggering. On the other hand, in synchronous trigger mode the external trigger signal is used not only as a starting signal, but when it is detected, the clock to the sensor is generated again in order to eliminate delay generation as much as possible. Since in *Pump & probe* experiments the most precise synchronization between signal chopping, pulses generation and acquisition is needed (in order to avoid partial acquisitions), we chose to work in synchronous mode.

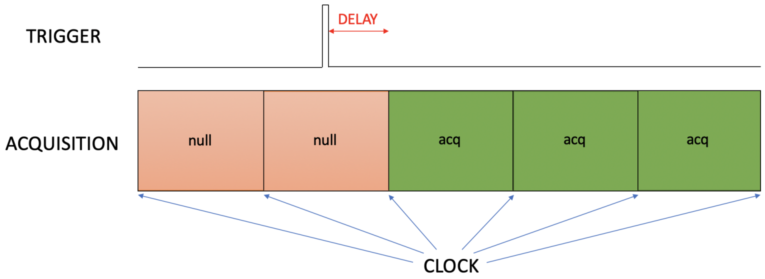

(a) *Asynchronous mode*

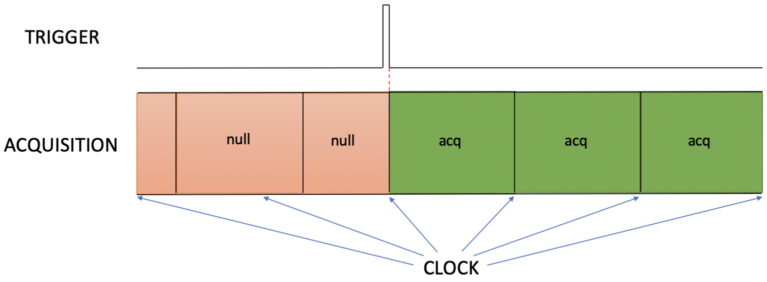

(b) *Synchronous mode*

Figure 3.6: Trigger synchronous and asynchronous mode. In synchronous mode the clock is synchronized with the trigger's detection, while in asynchronous mode this is not done causing the possibility to have a delay between the trigger's detection and the first acquisition.

### Edge sense trigger mode Vs Level sense trigger mode

There are two options to control the spectrometer acquisition based on the triggering signal: level mode and edge mode. In the first mode the spectrometer acquires only when the triggering signal is in a specified level (*high-level* or in *low-level* depending on the settings). In the second one the acquisition starts when there is an edge in the trigger signal (rising or falling depending on the settings) and then goes on until the computer gives a stopping command. The main difference between the two mode is that in level mode the duty cycle of the triggering signal has to be as long as the measurement duration, while in edge mode the end of the measurement process is given by a command from the computer. Having the need of averaging the result of a relatively high number of acquisition (40) in order to reduce noise, we chose to work in edge mode.

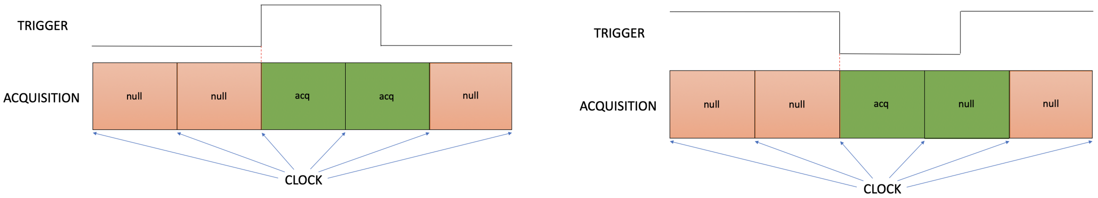

(a) *high-level* (b) *low-level*

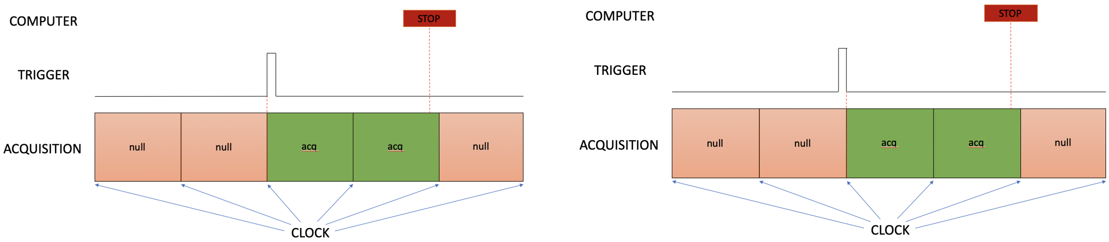

(c) *rising edge* (d) *falling edge*

Figure 3.7: Trigger level $\big((a)-(b)\big)$ and edge $\big((c)-(d)\big)$ modes. In level mode the duration of the measurement is controlled by the length of the duty cycle of the triggering signal, while in edge mode the trigger signal is used only to start the measurement which then has to be stopped by a command from the computer.

### 3.2.2 Labview program

The spectrometer comes with its own evaluation software, but in order to have full control on the acquisition process the constructor provides also a DLL library, which allows to build customized acquisition programs with different programming frameworks (Visual Studio, Visual C++ and LabVIEW). Since the acquisition programs in which the spectrometer acquisition had to be integrated are written with the LabVIEW[1] framework, I used this language.

---

[1] LabVIEW is a graphic programming framework developed by National Instruments and is mainly used in the industrial automation field for data analysis and acquisition.

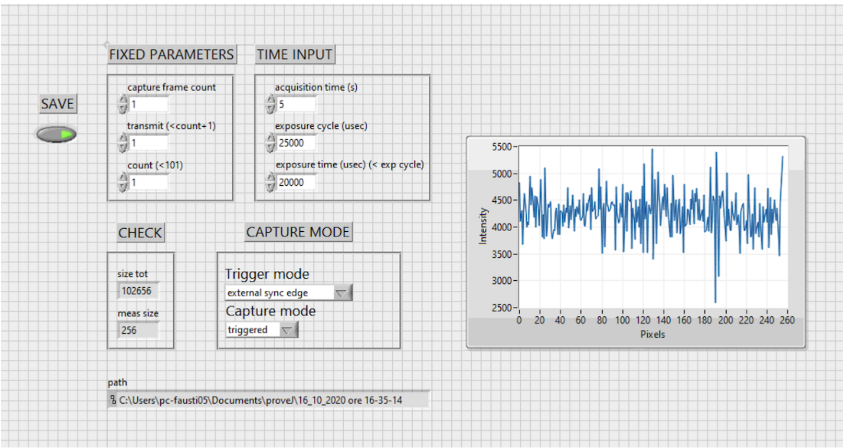

capture frame count
1
transmit (<count+1)
1
count (<101)
1
acquisition time (s)
5
exposure cycle (usec)
25000
exposure time (usec) (< exp cycle)
20000
size tot
102656
meas size
256
Trigger mode
external sync edge
Capture mode
triggered
path
C:\Users\pc-fausti05\Documents\proveJ\16_10_2020 ore 16-35-14

Figure 3.8: User interface of the LabVIEW program. It allows the user to select the operational mode to use (specified, continuous or triggered) and shows a live plot of the measured spectrum.

I will briefly explain the logical steps to make a proper use of the spectrometer.

- Initialization
    - *Device connection*: First of all, the computer has to identify the USB 2.0 port to which the spectrometer is connected.
    - *Temperature check*: Since the spectrometer is cooled type, it is necessary to check if the sensor has reached the working temperature of $-20\,^{\circ}\mathrm{C}$ before starting the acquisition.
    - *Parameters setting*: Reading the user's input, the parameters of the acquisition (exposure time, operational mode) are set.
    - *Buffer allocation*: The computer allocates a part of the RAM where the spectrometer saves the data acquired waiting for the computer to read them.
    - *Saving path*: Create a path to permanently save the result of the acquisition.
- Acquisition
    - *Capture start*: The computer gives a signal to the spectrometer to start the measurement.
    - *Buffer reading*: The computer reads the data acquired by the sensor saved in the buffer; if required elaborates them and then saves them in a txt file in the saving path.

NB The buffer reading step is looped for the duration of the entire measurement.

- Uninitialization
  - *Capture stop*: The computer gives to the spectrometer a signal to stop the measurement.
  - *Buffer deallocation*: The computer releases the RAM allocated as buffer.
  - *Device disconnection*: The computer correctly disconnects from the device, closing all processes in order to be able to reconnect without errors.

### 3.2.3 Timing of the experiment

Before designing the timing of the *Pump & probe* experiment (i.e. the frequencies of acquisition and chopping) the spectrometer's acquisition speed limits have to be understood. Each acquisition cycle consists of the following steps:

- *Exposure* (variable duration): Integration of the sensor.
- *A/D conversion* (2 ms): Digitalization, on the CMOS chip, of the continuous output of the sensor.
- *Buffer writing* ((10 – 20) ms): Data transfer to the computer via USB2.0.

While the exposure time can be set by the user (typically with duration of the order of ms), A/D conversion and buffer writing have an intrinsic duration that cannot be reduced, hence this gives a lower bound to the complete acquisition cycle time of roughly 20 ms [19].
Bearing that in mind, we designed the timing of the *Pump & probe* experiment starting from an acquisition rate of 40 Hz.

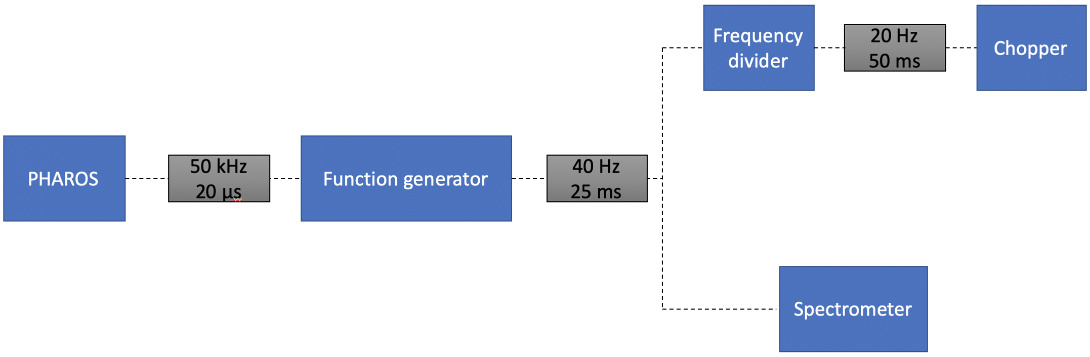

Figure 3.9: Trigger path. A trigger signal at 50 kHz is generated by the laser's electronics and then is passed to a function generator which returns the trigger signal used for the spectrometer at 40 Hz. The same signal divided by two is used to trigger the chopper's rotation.

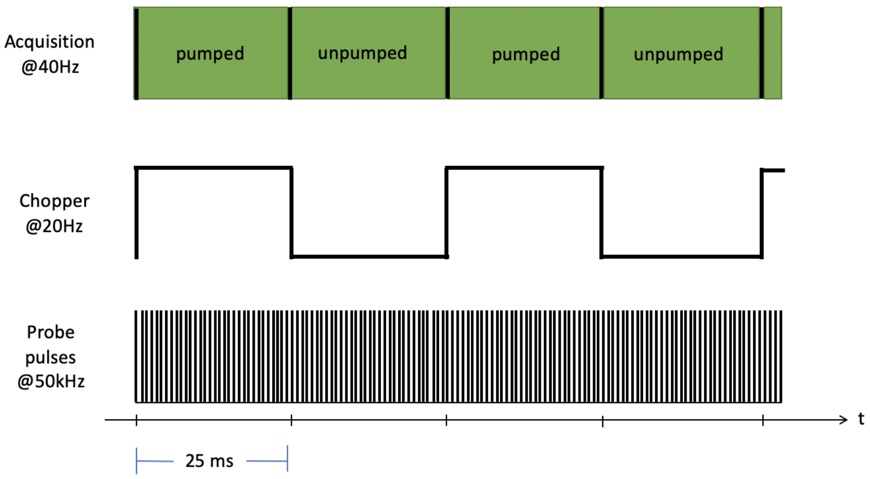

Figure 3.10: Experiment's timing. The chopping frequency is half of the acquisition's one in order to measure both pumped and unpumped signals. Each acquisition is the integration of many pulses (to be precise, with an exposure time of 5 ms 50 pulses at 50 kHz are integrated).

Each time a light pulse is emitted (hence at the working frequency of 50 kHz), the laser generates a trigger signal of 100 ns of duty cycle. This signal is used to trigger a function generator, which generates a square wave signal of 25 ms of period (hence a trigger frequency of 40 Hz). The acquisition of the spectrometer is triggered by this signal, while the chopper is triggered by a trigger with half of the frequency, in order to measure both the pumped and the unpumped signals (as can be seen in figures 3.9 and 3.10).

# Chapter 4

# Spectrometer characterization

In this chapter I will show the first set of measurements, performed to characterize the spectrometer's response. After measuring the background noise, we used quasi monochromatic near infrared pulses obtained with a Twin OPA to confront the response of the spectrometer with the nominal output wavelength of the system. Lastly, we used the spectrometer to investigate how to generate a white light probe with a spectral content broadened in the near infrared region.
All these measurements have been executed with the LabVIEW program described in section 3.2.2, in specified mode, averaging 40 single acquisitions (which corresponds to 1s of measurement at the fastest possible rate of 40 Hz, see section 3.2.3).

## 4.1 Background

First of all, we measured the background noise (which can be seen in figure 4.1) by uncovering the entrance slit of the spectrometer without shining any laser beam on it. We compared the results obtained using two different exposure times: 6 ms and 20 ms.

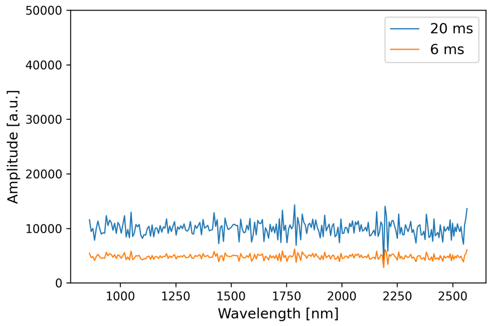

Figure 4.1: Background noise measured with both 6 ms (orange) and 20 ms (blue) of exposure time. These values showed to be constant in time.

The background measured was not a white noise, since it showed a dependence from the wavelength constant in time. This is why by integrating for longer exposure times the noise signal increases.

## 4.2 Detection of a tunable infrared beam

As our setup is provided with two infrared OPAs, we used their tunable outputs (ranging from 1300 to 2500 nm) to characterize the sensitivity of the spectrometer to different photon energies. We measured the output of both the OPAs at steps of 100 nm using an exposure time of 6 ms. The measurements after the subtraction of the background noise from figure 4.1 can be seen in figure 4.2.

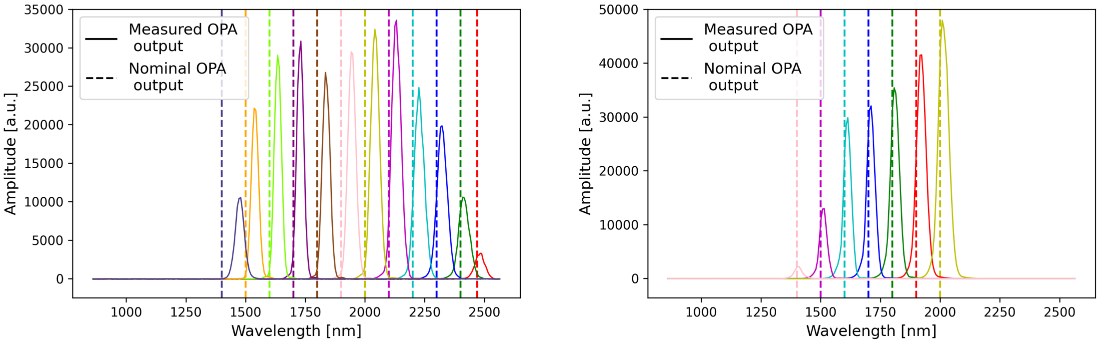

(a) *OPA 1*

(b) *OPA 2*

Figure 4.2: OPA's output at different wavelengths measured with an exposure time of 6 ms. The background noise has been subtracted. Dashed lines indicates the nominal output from the OPAs. A bias between measured and nominal output can be seen.

In particular, we can highlight the presence of an offset between the measured quasi-monochromatic peak and the nominal output indicated by the OPAs. Anyway, since the entity of this offset is different between the two OPAs (about 25 nm for OPA1 and 5 nm for OPA2), it is reasonable to suppose that this discrepancy is caused by calibration errors in the OPAs. Indeed, for these systems it is quite common that some internal misalignments lead to slightly different phase matching conditions on the crystal with respect to the desired ones.

Then, by means of a powermeter, we measured the power of the outputs from the OPAs at the different wavelengths. By dividing, for each peak, the spectrometer's response of figure 4.2 by the corresponding measured power and normalizing to the highest peak, we have been able to reconstruct the wavelength dependence of the spectrometer's response. As we can see from figure 4.3, this trend qualitatively matches the wavelength dependence of the sensor's relative sensitivity declared by the constructor and reported in figure 3.2.

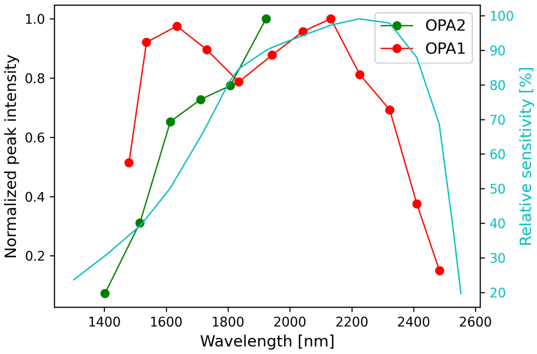

Figure 4.3: Comparison of the normalized peak intensities of the outputs from the two OPA's (green and red lines) with the declared [16] relative sensitivity (blue lines). The normalized intensities have been obtained by dividing the spectrometer's response by the corresponding measured power and normalizing it to the highest peak.

To conclude, we focused our attention on the 1400 nm output from the OPA2. Since it had a low intensity peak, we found it a good test bench to show how signal to noise ratio is influenced by the exposure time. To do so, we measured this beam with both 6 ms and 20 ms of exposure time (figure 4.4).

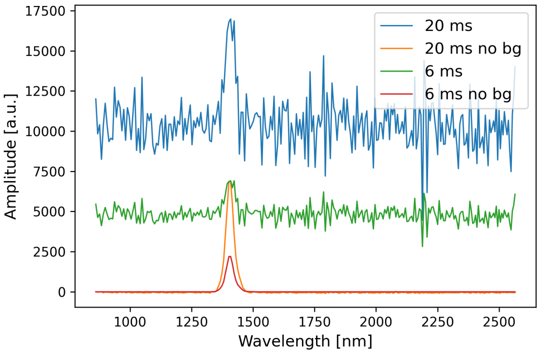

Figure 4.4: Comparison of the 1400 nm output (with and without subtracting the background) with an exposure time of 20 ms (blue and orange lines) and with one of 6 ms (green and red lines).

As we expected from the background measurements of section 4.1, changing the exposure time allows us to obtain only a slight increase in the signal to noise ratio. Anyway, if we subtract the background, the highest exposure time performs better (orange and red lines).

## 4.3 White light generation in the near infrared range

Until now we characterized the spectrometer's response to quasi monochromatic light beams, however in this last section I will report how we used it to investigate how we could generate white light probe pulses with a spectrum broadened in the near infrared region.
First, we studied the white light obtained by focusing a beam of pulses at 1030 nm directly from the Pharos system on a 6 mm long sapphire crystal.

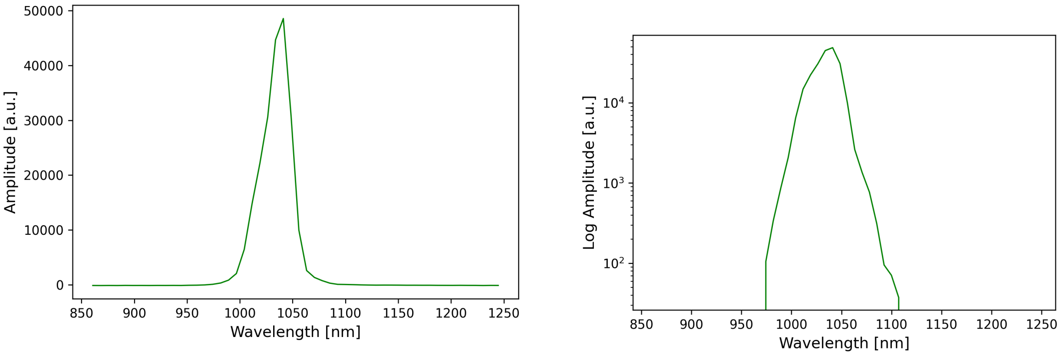

(a) *Linear scale* (b) *Logarithmic scale*

Figure 4.5: White light generation from sapphire crystal with a 1030 nm fundamental. Background has been subtracted.

As we can see from figure 4.5, there is nearly no white light generation in the near infrared region of the spectrum: indeed, as emerges from the logarithmic scale representation in 4.5 (b), we have a very small broadening band up to 1110 nm. This can be a consequence of the fact that since the temporal response time of the non linear term is of the order of $(1-10)$ fs [20], the front of the pulse is less influenced by self phase modulation, hence the conversion to higher wavelengths is less efficient. A possible solution to increase the broadening band could be to use a longer crystal.

After consulting the literature [21], we found that YAG crystals are more suitable for near infrared white light generation. Hence we studied the result of focusing a beam of pulses at 1500 nm on a 2 mm long YAG crystal. The white light generated is shown in figure 4.6.

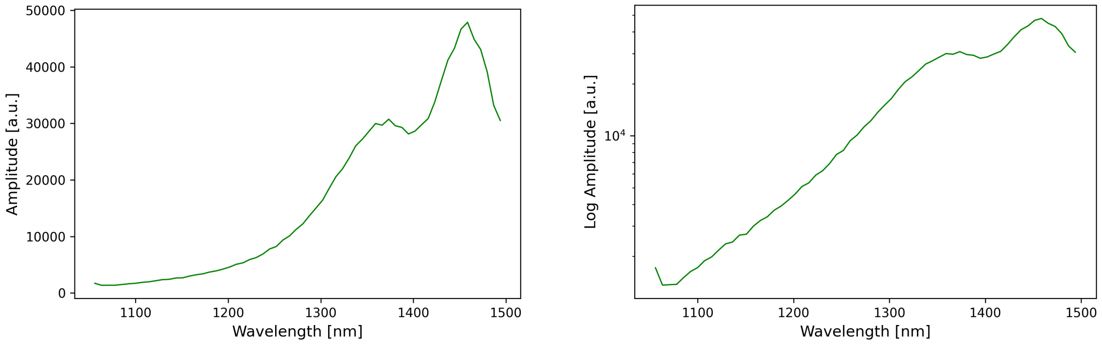

(a) *Linear scale* (b) *Logarithmic scale*

Figure 4.6: White light generation from YAG crystal with a 1500 nm fundamental. Background has been subtracted. These pulses contain wavelengths intense enough to be used as spectroscopic probe in a range from 1300 nm to 1500 nm

# Chapter 5

# Application: Pump & probe experiment with 1030nm probe on BSCCO

In this last chapter, I will illustrate the results obtained with the integration of the spectrometer in the experimental setup in figure 2.4 to perform time and frequency resolved *Pump & probe* reflectivity measurements at room temperature on a commonly studied cuprate: BSCCO. After a brief introduction on its crystalline structure (sections 5.1), I will show and discuss the experimental measurements (sections 5.2).

## 5.1 Crystalline structure

Bismuth-Strontium-Calcium-Copper-Oxide (abbreviated with BSSCO) is a family of compounds which contains some of the most studied superconducting cuprates. But not all its members are superconductors. Indeed, being the generalized formula of the family $Bi_2Sr_2Ca_{m1}Cu_mO_{2m+4+\delta}$, only the compounds with m=1,2,3 (where m represents the number of $Cu-O$ planes) show superconducting behaviour.
In particular, the sample used for the measurements, is a BSCCO with $m = 2$ (compound typically called Bi2212). This compound, which is the most studied of the family, has a perovskite-like crystal structure that can be seen in figure 5.1.

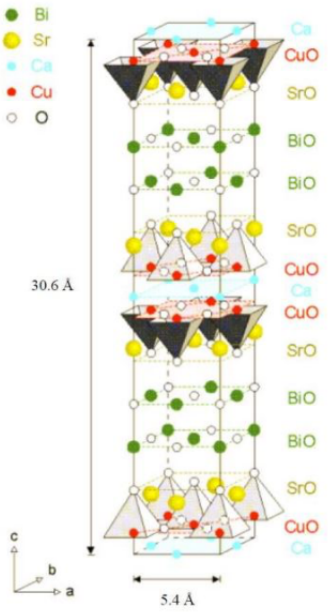

Figure 5.1: Bi2212 crystal structure

In the generalized formula of the family $\delta$ indicates the level of oxygen doping. The sample used for the experiments is an optimally doped compound.

## 5.2 Measurements

Figure 5.2 reports the measured transient reflectivity $\frac{\delta R}{R}(\omega, t)$, as defined in section 2.1, obtained as the average of 13 scans under the following conditions:

- pump fluence: 15 µJcm$^{-2}$
- pump wavelength: 450 nm
- probe wavelength: broadened 1030 nm[1]

As we can see from the irregular sign inversions in figure 5.2, the measurement is very noisy. A possible solution to this issue could be to add a reference beam to monitor and correct the probes fluctuation, like it has been done in [3]. Another feasible (and easier) way to increase the signal to noise ratio would be to increase the number of scans on which the average is made, which obviously comes at the cost of extending the duration of the measurement.

---

[1] See figure 4.4 for the probe spectrum.

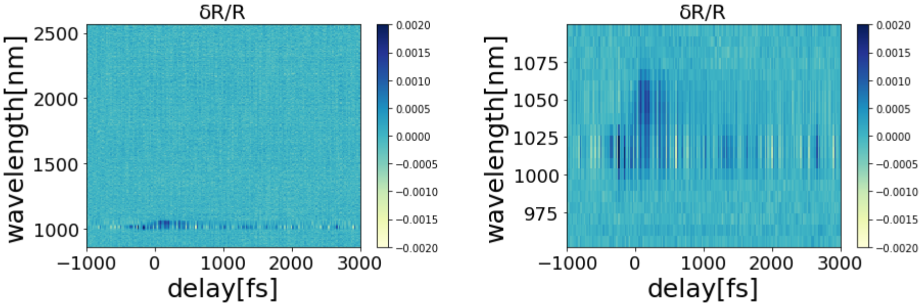

(a) (b)

Figure 5.2: Transient reflectivity at T=300K of BSCCO as a function of time delay between the probe and pump pulses (horizontal axis) and the probe's wavelength (vertical axis). As can be seen comparing (*a*) e (*b*), only a small part of the measured spectrum has been exploited.

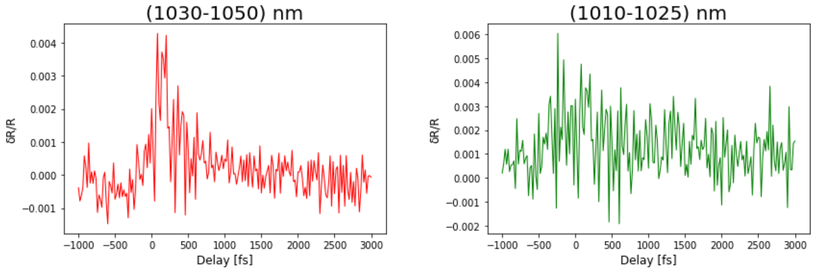

(a) *First trend* (b) *Second trend*

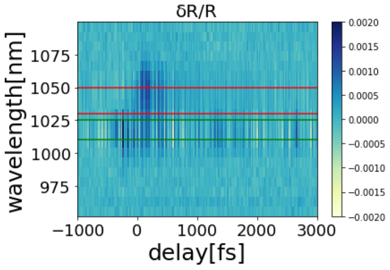

(c) *Cuts*

Figure 5.3: Wavelength cuts. The figure in (*a*) e (*b*) have been obtained from (c) by summing the values between the two lines.

Despite the low signal to noise ratio and the small spectral broadening of the probe, we can identify two different trends, which are highlighted by the horizontal cuts of figure 5.2. These cuts are obtained by summing the regions between the two lines (wavelength integration).

By comparing figure 5.2 (a) to similar measurements [22], we reckon that its double exponential decay, with a fast component of about 500 fs followed by a slower one, with a decay time of about 2 ps, can be interpreted as the thermalization of the photoexcited system by interaction with strongly-coupled phonons (sub-ps dynamics) and with the rest of the lattice (ps dynamics).
Further studies will be carried on to extend the measurements to longer wavelength with appropriate probes.

# Chapter 6

# Conclusions

For this thesis work the commissioning of an infrared spectrometer for applications in *Pump & probe* experiments has been realized.
After having analyzed in detail the components of *Pump & probe* experiments and the physical phenomena which they exploit (chapter 2) and after having understood the operational modes of the spectrometer (chapter 3), a LabVIEW program which allows both to use the spectrometer independently and to integrate it as part of a *Pump & probe* setup has been written.
Then, using the spectrometer as an independent tool, it has been characterized by measuring the output of a Twin-OPA in a wavelength range of $(1400 - 2500)\,\mathrm{nm}$. With the same operational mode, the spectral content of the probe in use on the setup has been measured. Since it showed up being quasi-monochromatic (figure 4.4 ), a more efficient near infrared white light generation process has been tested (figure 4.5).
Lastly, the integration of the spectrometer in the *Pump & probe* experimental setup of figure 2.5 has been showed by the realization of a *Pump & probe* experiment on a BSCCO sample at room temperature. The results of this measurements, presented in Chapter 5, leave room for improvement: the signal to noise ratio has to be increased, and the probe generated with $1030\,\mathrm{nm}$ pulses on the sapphire crystals has a too narrow spectral content which does not allow to have a broadband analysis of the transient reflectivity. Anyway, during the thesis we have identified a way to solve the issue of the narrow spectral bandwidth of the white light source: indeed, in chapter 4 we have shown that an ultrashort broadband laser pulse with larger spectral content in the near IR can be produced.
Solved these two problems, the spectrometer commissioned for this thesis work could become a useful tool which can be integrated in more complex *Pump & probe* experiments to further investigate the properties of high temperature superconductors.

# Bibliography

[1] E. Snider, N. Dasenbrock-Gammon, R. McBride, M. Debessai, H. Vindana, K. Vencatasamy, K. V. Lawler, A. Salamat, and R. P. Dias, "Room-temperature superconductivity in a carbonaceous sulfur hydride," *Nature*, vol. 586, no. 7829, pp. 373–377, 2020. [Online]. Available: https://doi.org/10.1038/s41586-020-2801-z

[2] C. Giannetti, M. Capone, D. Fausti, M. Fabrizio, F. Parmigiani, and D. Mihailovic, "Ultrafast optical spectroscopy of strongly correlated materials and high-temperature superconductors: a non-equilibrium approach," *Advances in Physics*, vol. 65, 01 2016.

[3] A. Montanaro, F. Giusti, M. Colja, G. Brajnik, A. M. A. Marciniak, R. Sergo, D. De Angelis, F. Glerean, G. Sparapassi, G. Jarc, S. Carrato, G. Cautero, and D. Fausti, "Visible pump–mid infrared pump–broadband probe: Development and characterization of a three-pulse setup for single-shot ultrafast spectroscopy at 50 khz," *Review of Scientific Instruments*, vol. 91, no. 7, p. 073106, 2020.

[4] F. Novelli, G. De Filippis, V. Cataudella, M. Esposito, I. Vergara, F. Cilento, E. Sindici, A. Amaricci, C. Giannetti, D. Prabhakaran, S. Wall, A. Perucchi, S. Dal Conte, G. Cerullo, M. Capone, A. Mishchenko, M. Grüninger, N. Nagaosa, F. Parmigiani, and D. Fausti, "Witnessing the formation and relaxation of dressed quasi-particles in a strongly correlated electron system," *Nature Communications*, vol. 5, no. 1, p. 5112, 2014. [Online]. Available: https://doi.org/10.1038/ncomms6112

[5] H. K. Onnes, "The superconductivity of mercury," *Comm. Phys. Lab. Univ., Leiden*, p. 122–124, 1911.

[6] J. G. Bednorz and K. A. Müller, "Possible hightc superconductivity in the $BaLaCuO$ system," *Zeitschrift für Physik B Condensed Matter*, vol. 64, no. 2, pp. 189–193, 1986.

[7] F. Giusti, A. Marciniak, F. Randi, G. Sparapassi, F. Boschini, H. Eisaki, M. Greven, A. Damascelli, A. Avella, and D. Fausti, "Signatures of enhanced superconducting phase coherence in optimally doped $Bi_2Sr_2Y_{0.08}Ca_{0.92}Cu_2O_{8+\delta}$ driven by midinfrared pulse excitations," *Phys. Rev. Lett.*, vol. 122, p. 067002, Feb 2019. [Online]. Available:

https://link.aps.org/doi/10.1103/PhysRevLett.122.067002

[8] C. Giannetti, F. Cilento, S. D. Conte, G. Coslovich, G. Ferrini, H. Molegraaf, M. Raichle, R. Liang, H. Eisaki, M. Greven, A. Damascelli, D. van der Marel, and F. Parmigiani, "Revealing the high-energy electronic excitations underlying the onset of high-temperature superconductivity in cuprates," *Nature Communications*, vol. 2, no. 1, p. 353, 2011. [Online]. Available: https://doi.org/10.1038/ncomms1354

[9] M. Fox, *Quantum optics: an introduction*, ser. Oxford master series in atomic, optical, and laser physics. Oxford: Oxford Univ. Press, 2006.

[10] R. W. Boyd, *Nonlinear Optics, Third Edition*, 3rd ed. USA: Academic Press, Inc., 2008.

[11] A. Siegman, *Lasers*. University Science Books, 1986. [Online]. Available: https://books.google.it/books?id=1BZVwUZLTkAC

[12] L. Conversion. Orpheus-n features. [Online]. Available: http://lightcon.com/uploads/datasheets/ORPHEUS-N%20datasheet%2020200602.pdf

[13] Hamamatsu. Mini-spectrometers. [Online]. Available: https://www.hamamatsu.com/resources/pdf/ssd/c11118ga_kacc1170e.pdf

[14] ——. Mini-spectrometers, technical information. [Online]. Available: https://www.hamamatsu.com/resources/pdf/ssd/mini-spectrometer_kacc9003e.pdf

[15] A. Rogalski, "Infrared detectors: An overview," *Infrared Physics Technology*, vol. 43, pp. 187–210, 06 2002.

[16] Hamamatsu. Characteristics and use of infrared detectors. [Online]. Available: https://www.hamamatsu.com/resources/pdf/ssd/infrared_kird9001e.pdf

[17] ——. Ingaas linear image sensors. [Online]. Available: https://www.hamamatsu.com/resources/pdf/ssd/g9211-256s_etc_kmir1011e.pdf

[18] Y. Gurevich and J. Velázquez-Pérez, *Peltier Effect in Semiconductors*, 04 2014, pp. 1–21.

[19] Hamamatsu. Mini-spectrometers trigger function specifications.

[20] N. Dubreuil. Nonlinear optics - introduction (lecture notes). [Online]. Available: http://paristech.institutoptique.fr/site.php?id=979&fileid=12326

[21] F. Silva, D. Austin, A. Thai, M. Baudisch, M. Hemmer, D. Faccio, A. Couairon, and J. Biegert, "Multi-octave supercontinuum generation from mid-infrared filamentation in a bulk crystal," *Nature communications*, vol. 3, p. 807, 05 2012.

[22] F. Cilento, "Non-equilibrium phase diagram of $Bi_2Sr_2Y_{0.08}Ca_{0.92}Cu_2O_{8+\delta}$ cuprate superconductors revealed by ultrafast optical spectroscopy," Ph.D. dissertation, 2010/2011.

[23] D. Fausti and various authors. Incept project scientific material. [Online]. Available: http://www.inceptproject.eu/scientific-material/

[24] N. Ashcroft and N. Mermin, *Solid State Physics*. Saunders College Publishing, 1976.